RSC Advances

PAPER

View Article Online
View Journal | View Issue

Cite this: *RSC Adv.*, 2026, **16**, 1078

Low-intensity pulsed ultrasound responsive phase-change nanoparticles loaded with rapamycin for targeted therapy of atherosclerotic plaques

Dandan Wang,†[a] Xiaojing Zhang,†[b] Lingpeng Tang,[c] Shengnan Wang,[b] Yifang He,[a] Jiamin Liu,[a] Yanli Wang,[a] Shijie Zhang,[a] Jiangqiong Lai*[d] and Guorong Lyu *[ae]

Received 3rd December 2025
Accepted 18th December 2025

DOI: 10.1039/d5ra09347c

rsc.li/rsc-advances

Atherosclerosis (AS), the primary cause of cardio-cerebrovascular diseases, is characterized by plaques that trigger acute ischemic events. Current therapies face challenges in targeted delivery and efficient local drug release, limiting precise diagnosis and treatment. To address this, we developed an ultrasound-responsive nanosystem for integrated AS diagnosis and therapy. The nanosystem, based on polylactic-*co*-glycolic acid (PLGA), encapsulates perfluoropentane (PFP) and rapamycin (RAP), and is surface-modified with PP1 peptide (PPP@RAP NPs). The NPs exhibited an average size of 162.63 nm and a drug loading capacity of 36.95%, demonstrating excellent targeting ability. Low-intensity pulsed ultrasound (LIPUS) induced the phase transition of PFP, enhancing ultrasound signals by 85.64% and enabling controlled drug release. *In vivo* studies showed a significant reduction in lesion lipid area by 25.99% ($P < 0.001$), highlighting the therapeutic efficacy of the nanosystem. This ultrasound-triggered, peptide-targeted strategy integrates imaging and therapy, offering a promising approach for precise AS intervention with significant clinical translational potential.

Introduction

Atherosclerosis (AS) is a vascular inflammatory disease closely related to hemodynamic disorders.[1] As a primary contributor to cardio-cerebrovascular diseases,[2] AS plaques play an important role in the pathogenesis of life-threatening events such as stroke and myocardial infarction.[3] Plaques are characterized by the accumulation of lipids, cholesterol, and inflammatory cells within the arterial wall, leading to the formation of a necrotic core surrounded by a fibrous cap.[4] Currently, clinical management strategies for AS plaques include pharmacological treatments (*e.g.*, statins)[5] and invasive treatments such as angioplasty and stenting. However, systemic drug administration may lead to off-target effects on healthy tissues and variable treatment efficacy. Invasive treatments are associated with problems such as restenosis and thrombosis.[6] Despite these advancements, there remains a pressing need for more targeted and effective therapeutic strategies to address the AS plaques.

Advances in ultrasound molecular imaging have opened up a whole new path for the integration of diagnosis and treatment of AS plaques. While current therapeutic strategies, including macrophages-targeted therapies[7,8] and statin-encapsulated nanoparticles (NPs),[9] have shown promise, they are limited by slow onset of action and lack of local specificity, posing challenges for concurrent diagnostic and therapeutic applications. Additionally, although rapamycin (RAP) has demonstrated potential in inhibiting plaque progression through its immunosuppressive,[10] systemic administration often leads to dose-dependent side effects,[11] and its efficacy in achieving targeted plaque accumulation remains suboptimal.

To address these limitations, we propose to utilize phase-change NPs encapsulating perfluorocarbons (PFCs) to induce acoustic droplet vaporization (ADV) effect[12] under the excitation of low-intensity pulsed ultrasound (LIPUS). A liquid–gas phase transition occurs inside the NPs, leading to the rapid expansion, rupture, and subsequent drug release. The associated cavitation effects and other physical mechanisms induced by LIPUS facilitate precise local drug delivery,[13] significantly enhancing the therapeutic efficacy compared to conventional NPs. This strategy builds upon previous research demonstrating the effectiveness of low-intensity focused ultrasound (LIFU) combined with drug-loaded phase-transitional NPs in

[a]*Department of Ultrasound, The Second Affiliated Hospital of Fujian Medical University, No. 34 North Zhongshan Road, Quanzhou, Fujian Province, 362000, China. E-mail: lgr_feus@sina.com*

[b]*Second Clinical Medical College, Fujian Medical University, Quanzhou, Fujian Province, 362000, China*

[c]*Department of Ultrasonography, Shengli Clinical Medical College of Fujian Medical University, Fujian Provincial Hospital, Fuzhou University Affiliated Provincial Hospital, Fuzhou, Fujian, 350001, China*

[d]*Department of Ultrasound, The 910 Hospital of the Chinese People's Liberation Army Joint Logistic Support Force, No. 180 Huayuan Road, Quanzhou, Fujian Province, 362000, China. E-mail: Fj180ljq@sina.com*

[e]*Departments of Medical Imaging, Quanzhou Medical College, Quanzhou, 362000, China*

† These authors contributed equally.

thrombolysis.[14,15] To further improve targeting precision, the 16-mer Peptide PP1, which specifically recognizes scavenger receptor A (SR-A) highly expressed on the surface of foam cells,[16,17] is incorporated in to the NP design. This allows for targeted delivery to the atherosclerotic lesions. Moreover, NPs are phase-transformed when exposed to LIPUS, generating strong acoustic reflection and scattering signals, which enables localized drug therapy while also providing long-circulating triggerable contrast agents for ultrasound imaging.

In this study, we propose to construct targeted phase-change NPs loaded with RAP, perfluoropentane (PFP) and using PLGA, which has excellent biocompatibility and biodegradability,[18] as a carrier combined with PP1 to target SR-A1(PLGA-PP1-PFP@RAP) (Visual Abstract). These nano-sized NPs are targeted to foam cells on the vulnerable plaques in the blood circulation. Upon exposure to LIPUS, the NPs undergo a phase transition, releasing the encapsulated drug and acting precisely on the vulnerable plaque. We evaluated the characterization and safety of NPs, systematically explored the efficacy of LIPUS combined with phase-change NPs for the co-treatment of AS plaques. Furthermore, we investigated the mechanism of LIPUS for the treatment of AS. The imaging ability of NPs *in vitro* and *in vivo* was also evaluated. Collectively, this integrated platform represents a significant advancement towards developing an efficient, precise, safe, and effective NP-based system for the treatment of AS plaques, overcoming the limitations of current therapies and maximizing the local therapeutic impact of drug.

Methods

Materials and animals

PLGA (MW 15000, 50 : 50) was purchased from Daigang Bio Engineer Co., Ltd (Shandong, China). PFP was obtained from J&K Scientific Co., Ltd (Beijing, China). RAP was supported by Yuanye Bio-Technology Co., Ltd (Shanghai, China). 1-Ethyl-3-(3-dimethyllaminopropyl)-carbodiimide hydrochloride (EDC) and *N*-hydroxysuccinimide (NHS) was provided by Aladdin Reagent Co., Ltd (Shanghai, China). PP1 was purchased by GL Biochem Co., Ltd (Shanghai, China). 1,1′-Dioctadecyl-3,3,3′,3′-tetramethylindotricarbocyanine iodide (DiR), oxidized low-density lipoprotein (ox-LDL) and the Cell Counting Kit-8 (CCK-8) assay kit were obtained by Solarbio Science & Technology Co., Ltd (Beijing, China). Flurescein Isothiocyanate (FITC) was purchased from MCE (Shanghai, China). Hoechst 33342 dye and Hematoxylin and eosin (H&E) staining kit was purchased by Beyotime Biotechnology Co., Ltd (Shanghai, China). MMP-9 recombinant rabbit monoclonal antibody, CD68 recombinant rabbit monoclonal antibody were purchased from HUABIO Co., Ltd (Hangzhou, China). F4/80 antibody was purchased from Abcam (UK). SR-A1 polyclonal antibody was purchased by Proteintech Group (Wuhan, China). 4,6-diamidino-2-phenyindole dilactate (DAPI) was obtained from Borf Biotechnology Co., Ltd (Wuhan, China). Enzyme-linked immunosorbent assay (ELISA) kits, TdT-mediated dUTP nick-end labeling (TUNEL) apoptosis assay kits were purchased from Boster Biological Technology Co., Ltd (Wuhan, China).

Murine-derived macrophage RAW 264.7 cells and human umbilical vein endothelial cells (HUVECs) were purchased from Haixing Biosciences (Suzhou, China). C57BL/6 mice (6–8 weeks, 18–22 g) were obtained from Fuzhou Wu's Laboratory Animal Center (Fuzhou, China) and Male apolipoprotein E deficient ($ApoE^{-/-}$; 8 weeks, 25–28 g) mice and were purchased from ShuLaiBao Biotech Co., Ltd (Wuhan, China). All experiments in our study were approved by the Laboratory Animal Institutional Review Committee of Second Affiliated Hospital of Fujian Medical University (No. 2025231) and were performed in accordance with the institutional guidelines.

Synthesis of NPs

We first prepared untargeted and drug-free NPs. The organic phase was obtained by taking PLGA (25 mg) dissolved in dichloromethane (2 mL) at room temperature and 5% polyvinyl alcohol (PVA) was prepared as the aqueous phase. PFP (200 μL) was dropped into the organic phase in an ice bath. A mixed solution was obtained by ultrasonication (Sonics & Materials Inc., USA) with the power of 100 W for 5 min (5 s on/off). After that, slowly add 5%PVA into the solution and again using ultrasonication of 100 W for 10 min (5 s on/off). 2% isopropanol(10 mL) was added to the solution and magnetically stirred at room temperature for 4-6 h to fully evaporate the organic solvent. Subsequently, the solution was centrifuged at 10 000 rpm, 4 °C for 10 min and washed three times with phosphate-buffered saline (PBS, PH 7.4). Then the drug-free and non-targeted NPs (PLGA-PFP NPs, PP NPs) were harvested.

To further obtain the targeted nanoparticles, based on PP NPs, EDC/NHS solution was prepared as a coupling agent by the carbodiimide method. EDC/NHS and PP1 were added into the PP NPs solution at 4 °C (EDC/NHS : PP1 = 5 : 1). Then the mixture was placed on a shaker at 4 °C with slow shaking for 2 h to allow the activate the carboxyl groups and PP1 to be fully engaged. To remove unbound and excess reactants, the solution was again ultrafiltrated by centrifugation (4 °C, 8000 rpm, 10 min) and washed in PBS. The solution was obtained as PLGA-PFP-PP1 NPs (PPP NPs).

The drug-loaded NPs (PPP@RAP NPs) were obtained by dissolving an appropriate amount of RAP with PLGA in dichloromethane (2 mL), followed by the same procedure as that for the preparation of PPP NPs. The NPs could be labeled with DiR when the PLGA was dissolved in dichloromethane for subsequent fluorescence imaging. All the prepared NPs were stored at 4 °C for later use.

Characterization of NPs

The NPs internal structure was analyzed with a transmission electron microscope (TEM) (H-7600, Hitachi, Tokyo, Japan). The mean particle size, ζ potential and polydispersity index (PDI) were determined by dynamic light scattering (DLS) (Malvern Instruments, UK), and the NPs were measured repeatedly on days 1, 3, 5, 7, 14 to assess the stability of the NPs. Also we observed the appearance of various NPs solution with the naked eye within 48 h.

Determination of PP1 binding rate

Peptide PP1 was first labeled with FITC. The FITC-labeled peptide PP1 was then bound to DiR-pre-labeled PP NPs. After three washes, the dual-labeled nanoparticles were resuspended in ddH2O. Fluorescence images were acquired using a fluorescence microscope (Nikon, Japan). The conjugation rate between peptide PP1 and PP NPs was determined using a flow cytometer (B75442, Beckman, Shanghai), with quantitative analysis performed *via* FlowJo 10.8.1 software.

Drug loading and *in vitro* drug release of PPP@RAP NPs

To calculate the loading efficiency of RAP, an appropriate amount of RAP was dissolved in DMSO and diluted into different concentrations of RAP solutions. The absorbance of different concentrations of RAP solutions at 280 nm was detected by UV-vis spectrophotometer (Thermo Fisher, USA) and established the RAP standard curve. The drug loading capacity (LC) and drug encapsulation efficiency (EE) of PPP@RAP NPs were measured by lyophilization and calculated as the following equations.

$$\mathrm{LC}(\%) = \left(\frac{\text{RAP contents in the NPs}}{\text{Total mass of PPP@RAP NPs}}\right) \times 100$$

$$\mathrm{EE}(\%) = \left(\frac{\text{RAP contents in the NPs}}{\text{Total amount of RAP added}}\right) \times 100$$

To further evaluate the drug release ability of PPP@RAP NPs *in vitro*. 1 mL of drug-loaded NPs were irradiated with LIPUS (Chongqing Ronghai Ultrasound Medical Engineering Research Center, Chongqing, China) for 20 min. After irradiation, the NPs were sealed in a dialysis bag (MWCO 3500 Da) and placed in a PBS solution (20 mL) and stirred at 4 °C. The other group of 1 mL drug-loaded NPs without LIPUS irradiation were sealed directly in the dialysis bag in the medium with agitation. 200 μL of dialysate was collected from both groups of NPs at different time (1 h, 2 h, 4 h, 6 h, 12 h, 24 h, 48 h and 72 h) and immediately supplemented with 200 μL of fresh PBS, keeping the volume of solution constant. The cumulative drug release curve was plotted by detecting the absorbance value of the collected solutions at 280 nm by UV-vis spectrophotometer.

The assessment of the ADV effect *in vitro*

In order to evaluate the phase transition ability of NPs, the influence of the ADV effect on ultrasound-enhanced imaging signals generated by NPs after excitation by LIPUS was investigated. Firstly, an agarose gel imaging matrix model (agarose powder : deionized water = 1 : 50) was prepared according to the method of Mu *et al.*[19] NPs wrapped with PFP were dropped into the clot, and the irradiated using LIPUS (frequency 1.0 MHz, duty cycle 20%, spatial-average temporal-average intensity (I_{SATA})100 mW cm^{-2}, 20 min). The two-dimensional ultrasound images and contrast-enhanced ultrasound (CEUS) images of the NPs before irradiation, 5 min, 10 min and 20 min after irradiation were collected. Ultrasound images were recorded and stored by Mindray Resona I9 (Shenzhen, China) with a probe frequency of 8.5–14.5 MHz. Quantitative analysis of signal intensity were calculated using ImageJ software (National Institutes of Health, USA).

Cell culture and foam cell induction

Culture of RAW 264.7 cells and HUVEC cells: cultured in high sugar DMEM with 10% fetal bovine serum (FBS) and 1% penicillin-streptomycin added, placed in an incubator with 5% CO_2, 37 °C. The cells were observed under a light microscope, and when the cell density reached 80–90% the cells could be passaged or the next experiment could be carried out.

Foam cell induction: when the density of RAW 264.7 cells reached about 50%, the cells were treated with ox-LDL at 25 mg L^{-1} concentrations and placed at 37 °C with 5% CO_2 for 24 h.

Exploration of the best parameters of LIPUS and safety assessment of NPs

According to current literature research,[20] the frequency of LIPUS 1 MHz, the repetitive pulse frequency 1 kHz, duty cycle 20% and the pulse width 200 μs were set as fixed parameters. We explored the I_{SATA} and exposure time (ET). RAW 264.7 cells were seeded in a 3.5 cm dish. After the cells attached to the wall, they were placed on an irradiation plate and irradiated with different I_{SATA} and ET. After irradiation, place it back into the incubator and continue to incubate for 12 hours. Cell viability was evaluated using the CCK-8 at the end of the incubation period as the following equation

$$\text{Cell viability}(\%) = \left[\frac{(A_s - A_b)}{(A_c - A_b)}\right] \times 100\%$$

In which A_s is the absorbance value of the test group, A_b is the absorbance value of the blank group, and A_c is the absorbance value of the control group.

In vitro safety assessment (CCK-8): RAW 264.7 cells and HUVEC cells were inoculated in 96-well plates at a cell density of 1×10^5 per well for 12 h. Then, the cells were incubated with different concentrations of PPP NPs and PPP@RAP NPs to evaluate the *in vitro* safety. The well plates were removed at 4 h and 24 h of incubation, the medium was aspirated and the plates washed with PBS. Subsequently, 100 μL of medium and 10 μL of CCK-8 were added, and incubation was continued for 2 h. The OD value of the cells at 450 nm was detected by an enzyme labeled instrument (SPECTRA max, Molecular Devices, USA), and the cell survival rate was calculated.

In vivo safety assessment: 12 healthy male C57BL/6 mice were randomly divided into 4 groups: control, 1 d, 7 d and 14 d groups ($n = 3$). All mice except control group were injected with PPP@RAP NPs (200 μL, 5 mg kg^{-1}) *via* tail vein. Three mice were randomly selected for euthanasia at different time points (pre-injection, 1 d, 7 d and 14 d post-injection) and blood was collected for biochemical assays (including ALT, AST, ALB, CREA and BUN levels). Major organs (heart, liver, spleen, lungs and kidneys) of the mice were collected, fixed with 4% paraformaldehyde and stained with H&E.

Animal model

Male ApoE$^{-/-}$ mice (8 weeks) were given a high-fat diet (HFD) fed for 12 weeks to establish an atherosclerotic plaque model.

Evaluation of targeting capability

Validation of NPs targeting ability *in vitro*. Successfully induced foam cells, RAW 264.7 were inoculated in two six-well plates, respectively. After being adhered to the wall, incubated with DiR-PPP NPs or DiR-PP NPs (1 mg mL^{-1}) for 4 h. After incubation, the culture medium was discarded and washed with PBS. Added Hoechst 33342 (1 mL) staining solution incubated with the cells for 15 min, which was pipetted and then rinsed again with PBS. Finally, 1 mL of PBS was added and image acquisition using an inverted fluorescence microscope.

NPs uptake by RAW 264.7 cells *in vitro*. RAW 264.7 cells in the logarithmic growth were seeded into 12-well plates and cultured until they reached confluence, DiR-labeled PPP NPs (50 μL) were added to the cells and co-incubated in an incubator for 1 h, 2 h, 4 h, and 6 h. Cells were then washed three times with PBS and stained with Hoechst 33342 (1 mL). Following staining, fluorescence images were acquired using a fluorescence microscope. Cell uptake rates of NPs at different time points were determined by flow cytometry and quantified using FlowJo 10.8.1 software.

***In vivo* targeting and biodistribution of NPs.** *In vivo* targeting: 18 modeled ApoE$^{-/-}$ mice were randomly divided into two groups of 9 mice each and injected with DiR-labeled PP NPs and PPP NPs (200 μL) *via* tail vein. At three time points after injection (1 h, 2 h and 4 h), three mice were randomly taken from both groups. The entire aorta was removed by dissected after execution of the mice and washed the entire aorta with PBS solution. Subsequently, aortic fluorescence imaging was observed in each group using a small animal *in vivo* three-dimensional imaging system (AniView Kirin, Guangzhou, China), and the average fluorescence intensity of the aorta was quantified by Image J. The aortic fluorescence intensity of the aorta in each group was measured and analyzed.

In vivo biodistribution: Three modeled ApoE$^{-/-}$ mice were randomly selected and injected with DiR-PPP NPs (200 μL) *via* tail vein. Twenty-four hours after injection, the mice were executed and dissected, and the hearts, livers, spleens, lungs, and kidneys were removed, washed with PBS solution, and the fluorescence of each isolated organ was observed using a small animal *in vivo* three-dimensional imaging system to detect the *in vivo* biodistribution of the NPs.

Ultrasound imaging of ADV effects in NPs *in vivo*. Six modeled ApoE$^{-/-}$ mice were selected and randomly divided into two groups. DiR-labeled PP NPs and PPP NPs (200 μL) were injected *via* tail vein. Two hours after injection, mice were gas-anesthetized using isoflurane (RWD, Shenzhen, China). Ultrasound 2D and CEUS images were acquired by Mindray Resona I9 ultrasound diagnostic instrument with a probe frequency of 14 MHz. Subsequently, LIPUS irradiation (100 mW cm^{-2}, 20 min) was applied to the sternum of mice in both groups, and the 2D and CEUS ultrasound images were acquired again.

After completion of ultrasound imaging, both groups of mice (DiR-PP NPs non-targeted and DiR-PPP NPs targeted) were executed, and the entire aorta was dissected and removed. Frozen sections were prepared for immunofluorescence staining, F4/80 antibody staining for detection of macrophages, and DAPI re-staining of cell nuclei. The targeting of DiR-PP NPs and DiR-PPP NPs to plaques *in vivo* was further observed. Inverted fluorescence microscope was used to collect images.

Assessment of treatment effectiveness

***In vitro* therapeutic effect of NPs.** The induced foam cells were divided into blank, NPs, LIPUS and LIPUS + NPs groups. RAW 264.7 cells were used as control group. After 24 h of intervention treatment, the effect of NPs on foam cells was assessed using cell oil red O staining; meanwhile, the treated cells in each group were collected and the mRNA expression levels of TNF-α, IL-1β and iNOS inflammatory factors in foam cells were detected using qPCR. The relevant primer sequences are shown in SI Table 1.

Treatment and effect evaluation of AS ApoE$^{-/-}$ mice. The modeled AS ApoE$^{-/-}$ mice were randomly divided into 4 groups (9 mice in each group): (1) control group (2) PPP@ RAP NPs group (3) LIPUS group and (4) PPP@RAP NPs + LIPUS group. Mice in groups 2 and 4 were injected with PPP@RAP NPs (200 μL, 5 mL kg^{-1}) *via* tail vein. In group 4, mice were gas-anesthetized with isoflurane after injection 2 h, placed in a supine position on a flat plate, and irradiated for 20 min using LIPUS (100 mW cm^{-2}, 1 MHz, duty cycle 20%). The LIPUS probe applied with ultrasonic couplant and pressed lightly on the top of the sternum of the mouse for irradiation. Group 3 mice were irradiated in the same way. The mice were treated once every 2 days for a total of 21 days. The timeline of mouse treatment is shown in Fig. 6A.

Mice in each group were weighed at different time points of treatment (0, 5, 10, 15 and 21 days). At the end of treatment, all mice were euthanized and blood and entire aorta collected. After blood centrifugation (3000 rpm, 15 min, 4 °C), mice in each group ($n = 3$) were randomly selected for the lipid assays, and the remaining mice were assayed for plasma concentrations of TNF-α, IL-6, and IL-1β using ELISA kits. The aortas of mice in each group were stained with H&E, ORO, and Masson staining for detection of lipid deposition area and collagen content. Immunohistochemical staining (CD68, MMP9, and SRA1) was also performed to detect the number of macrophages, stability, and foam cell expression at plaque lesions.

Statistical analysis. Statistical analysis was performed by GraphPad Prism 10 software. Data were expressed as mean ± standard deviation (SD). Comparisons between two groups were performed by independent samples *t*-test, while one-way ANOVA was used for comparisons between more than two groups. Statistical differences were characterized by $P < 0.05$, and significance levels are indicated as follows: non-significant (NS), $^{*}P < 0.05$, $^{**}P < 0.01$, and $^{***}P < 0.001$.

Results

NPs characterization and drug release evaluation

The NPs were characterized using TEM, which clearly revealed the structural morphology of each NP group, all exhibiting

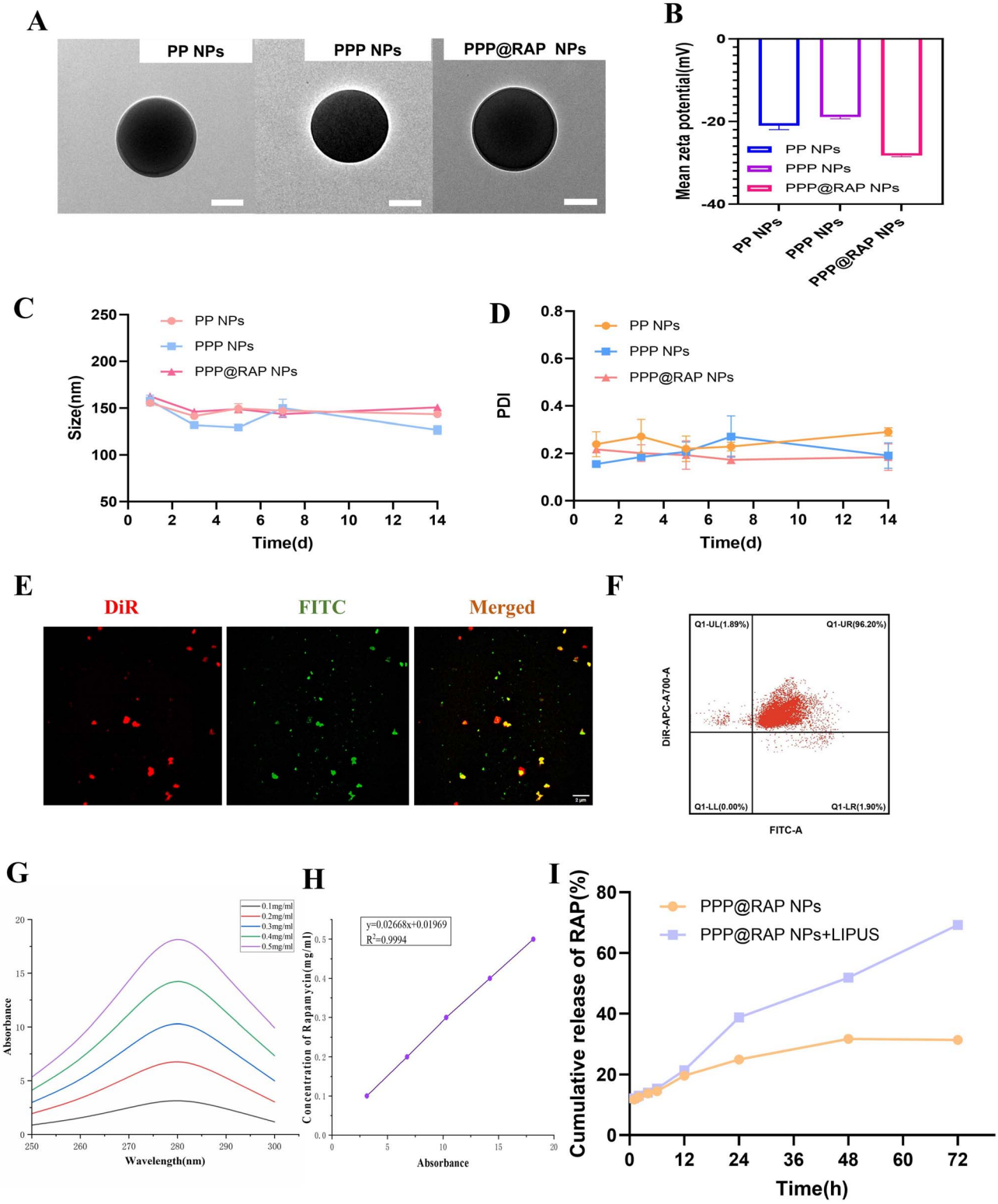

Fig. 1 Characterization of NPs (A) TEM images of PP NPs, PPP NPs and PPP@RAP NPs (scale bar = 50 nm). (B) Potential changes of the three NPs. (C) and (D) Dynamic comparison of particle size and PDI changes of the three groups of nanoparticles at days 1, 3, 5, 7, and 14. (E) Fluorescence image of peptide PP1 conjugated to PP NPs (scale bar = 2 μm). (F) Determination of the linkage ratio of peptides PP1 and PP NPs by flow cytometry. (G and H) Absorbance of RAP at different concentrations and the standard curve of RAP. (I) Drug release from PPP@RAP NPs with and without LIPUS irradiation. NPs: Nanoparticles, TEM: Transmission electron microscope, PDI: Polydispersity index, RAP: Rapamycin, LIPUS: Low-intensity pulsed ultrasound.

a uniform spherical structure with a smooth surface and no defects (Fig. 1A). The average diameter of PP NPs was approximately 125 nm, consistent with DLS results. The average particle size was (155.43 ± 2.79) nm, with a PDI of (0.24 ± 0.05) and a zeta potential of (−21.03 ± 1.63) mV (SI Table2). Linking the peptide PP1 increased the average size to 158.08 nm. Adding the drug RAP further increased the size to (162.63 ± 3.25) nm, with a PDI of (0.22 ± 0.01), indicating good dispersion. The PPP@RAP NPs exhibited a negative zeta potential of (−28.3 ± 0.46) mV (Fig. 1B), enhancing stability and reducing aggregation. The particle sizes remained within the ideal range (50–200 nm) and showed no significant changes over 14 days, with

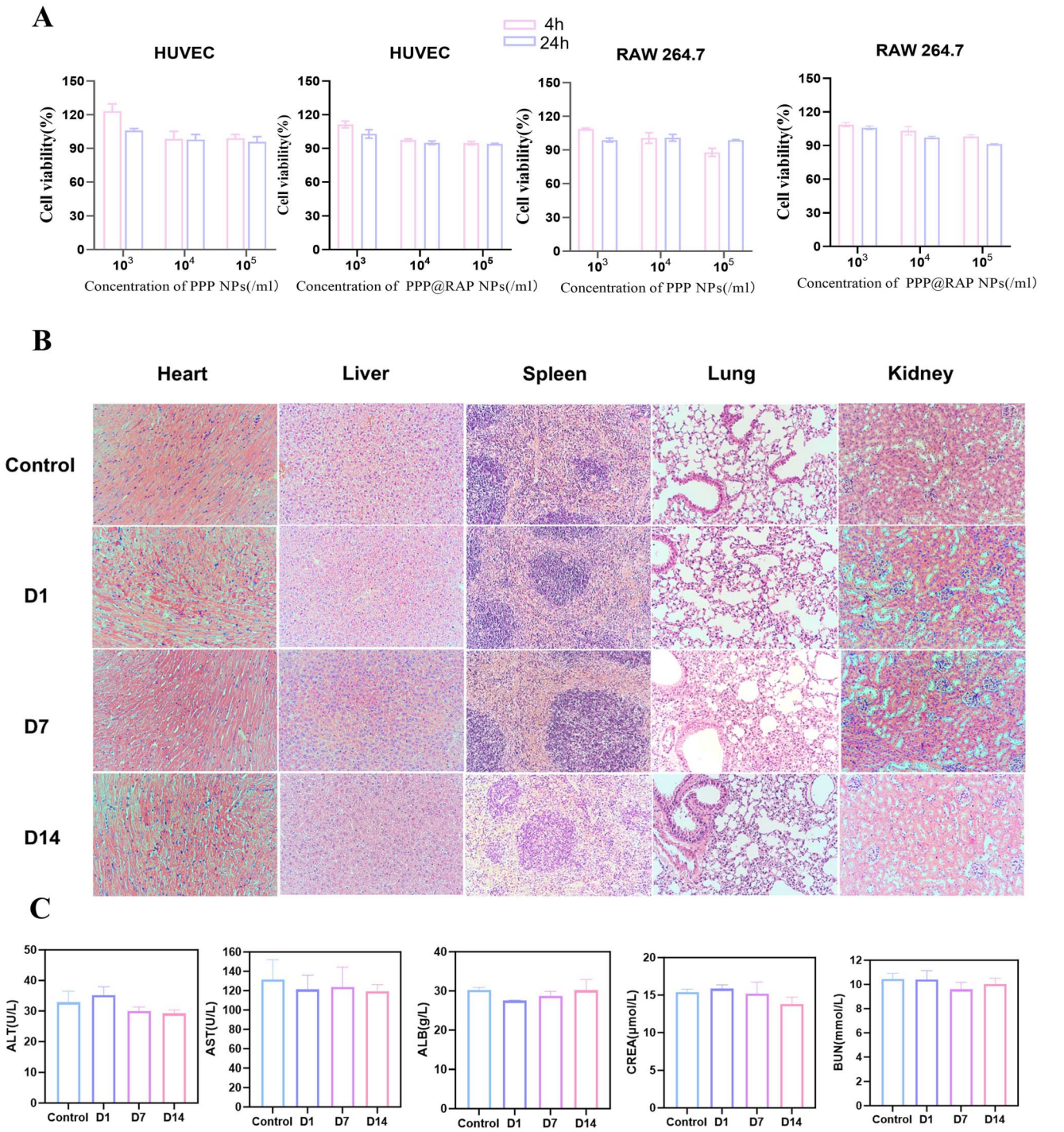

Fig. 2 Biosafety assessment of NPs (A) Cell viability profiles of HUVEC and RAW 264.7 cells following 4 h and 24 h incubation with PPP NPs and PPP@RAP NPs, respectively. (B) H&E stained sections (40× magnification) of major organs (heart, liver, spleen, lungs, and kidneys) collected at predetermined time intervals post PPP@RAP NPs administration. (C) Biochemical parameters reflecting liver (ALT, AST) and kidney (BUN, CRE) functions were measured at various time points following PPP@RAP NPs injection. NPs: Nanoparticles, H&E: Hematoxylin and eosin.

excellent dispersion (Fig. 1C and D). Visual observation confirmed no aggregation or precipitation in PBS, ddH2O, and 10% FBS solutions within 48 hours (SI Fig. S1C).

Fluorescence microscopy revealed distinct binding between peptide PP1 and PP NPs (Fig. 1E). Flow cytometry analysis demonstrated a binding efficiency of 96.20% between peptide PP1 and NPs (Fig. 1F and S1B). These results confirm the successful conjugation between NPs and peptide PP1.

The standard curve of RAP ($y = 0.02668x + 0.01969$, $R^2 = 0.9994$) was established by measuring the absorbance of RAP at different concentrations (Fig. 1G and H). LC of NPs was measured to be (36.95 ± 0.01)% and the EE was (64.67 ± 0.01)%. It proved that NPs had high LC and moderate EE. *In vitro* drug release studies showed that LIPUS irradiation significantly increased the drug release rate from 6 hours onwards, reaching a cumulative release of 69.30% at 72 hours (Fig. 1I). The initial release phase (0–4 hours) showed no significant difference between irradiated and non-irradiated groups, but the irradiated group exhibited enhanced release from 6 hours due to ultrasound-induced structural changes and the ADV effect.

Exploration of the best parameters of LIPUS and biosafety assessment of NPs

The frequency was set to 1 MHz for deeper penetration depth and effective induction of cavitation and ADV. The duty cycle of 20% was chosen to minimize thermal effects and avoid tissue overheating while maintaining sufficient mechanical effects. We mainly explored the I_{SATA} and Exposure Time (ET). RAW 264.7 cells were exposed to different ISATA values and irradiation times. The optimal parameters were determined to be 100 mW cm^{-2} and 20 minutes (SI Table 3), as this combination effectively induced phase transition of NPs and maintained a stable cavitation effect without excessive NP rupture or merging.

Different concentrations of PPP NPs and PPP@RAP NPs were co-incubated with RAW 264.7 and HUVEC cells, respectively. CCK-8 assay was performed on the cells after 4 h and 24 h of incubation. The results showed no significant cytotoxicity. The cell survival rate was more than 80% at all concentrations (Fig. 2A). At the animal level, we injected PPP@RAP NPs into healthy mice *via* the tail vein, and collected blood and organs after the mice were executed at different time points. The results of H&E staining of heart, liver, spleen, lungs and kidneys showed that none of the organs had obvious lesions such as infection and inflammation (Fig. 2B). In addition, we detected ALT, AST, ALB, CREA and BUN in the mice, which were all at normal levels, suggesting that the liver and kidney functions of the mice were not impaired (Fig. 2C).

The ADV effect assessment *in vitro*/vivo

In vitro ADV effect assessment used PBS as a control. Under low-intensity pulsed ultrasound (LIPUS, 100 mW cm^{-2}) irradiation, PP NPs showed stronger acoustic intensity in both B-mode ultrasound and CEUS images compared to the control group, peaking at 10 minutes ($P < 0.001$), followed by a slight decrease at 20 minutes (Fig. 3A). Statistically significant differences were observed at all time points (0, 5, 10, and 20 minutes) ($P < 0.001$) (Fig. 3B). In *in vivo* assessment, PP NPs and PPP NPs were injected *via* tail vein, respectively, followed by LIPUS irradiation 2 hours after injection. The CEUS signal of the group injected with PPP NPs after irradiation increased by 85.64% compared to before irradiation ($P < 0.001$), significantly higher than that of the group injected with PP NPs ($P < 0.001$) (Fig. 3C), confirming efficient ADV effects both *in vitro* and *in vivo*.

Targetability evaluation

***In vitro* NPs targeting and uptakes.** Labeled fluorescent non-targeting NPs (DiR-PP NPs) and targeting NPs (DiR-PPP NPs) were incubated with RAW 264.7 cells and foam cells, respectively. Fluorescence results showed that DiR-PPP NPs only aggregated around foam cells without significant binding in RAW 264.7 cells. While non-targeted DiR-PP NPs showed no significant binding in both RAW 264.7 and foam cells (Fig. 4A). The fluorescence intensity of targeted nanoparticle internalization by foam cells was significantly higher than that of non-foam cells and non-targeted nanoparticles ($P < 0.001$) (Fig. 4C). Fluorescence microscopy further validated NPs uptake, showing consistent uptake at different time points, with a peak at 2 hours followed by a decline at 4 hours (Fig. 4B). Quantitative fluorescence analysis also corroborated this result, and the fluorescence intensity taken up by cells at 2 h was statistically different from that at other time points ($P < 0.001$) (Fig. 4D). Flow cytometry analysis confirmed cellular uptake rates of 23.1%, 61.5%, 45.8%, and 35.7% at 1 h, 2 h, 4 h, and 6 h, respectively (Fig. 4E). The results of flow cytometry were further corroborated by the results of fluorescence analysis.

***In vivo* target plaque capacity and biodistribution.** We verified by both body-view microscopy and ultrasound that atherosclerotic plaque was observed in both the aortic arch and abdominal aorta of $ApoE^{-/-}$ mice after 12 weeks of high-fat diet (SI Fig. S2). To validate the targeting ability of NPs to foam cells, ex vivo aortic fluorescence images were obtained from AS mice injected with DiR-PP NPs and DiR-PPP NPs at 1 h, 2 h, and 4 h post-injection (Fig. 5A). The aortic fluorescence intensity in mice administered with targeted NPs was significantly higher than that in mice receiving non-targeted NPs. Statistical analysis confirmed significant differences in fluorescence intensity between targeted and non-targeted group ($P < 0.01$) (Fig. 5B). Immunofluorescence staining analysis was performed on three AS model mice after injecting targeted and non-targeted nanoparticles (NPs), respectively. The results showed that the targeted DiR-PPP NPs (red fluorescence) co-localized with macrophages (green fluorescence), indicating that they could effectively target and penetrate plaques; while no red fluorescence was observed in the non-targeted NPs group (Fig. 5C). Statistical analysis further showed that the fluorescence intensity within the plaque in the targeted PPP NPs group was significantly higher than that in the non-targeted PPP NPs group ($P < 0.01$) (Fig. 5D), confirming its good targeting performance.

At 24 h post-injection, ex vivo fluorescence imaging was performed on major organs of three randomly selected mice in the targeted NPs group (Fig. 5E). Quantitative analysis results revealed predominant NPs accumulation in the liver.

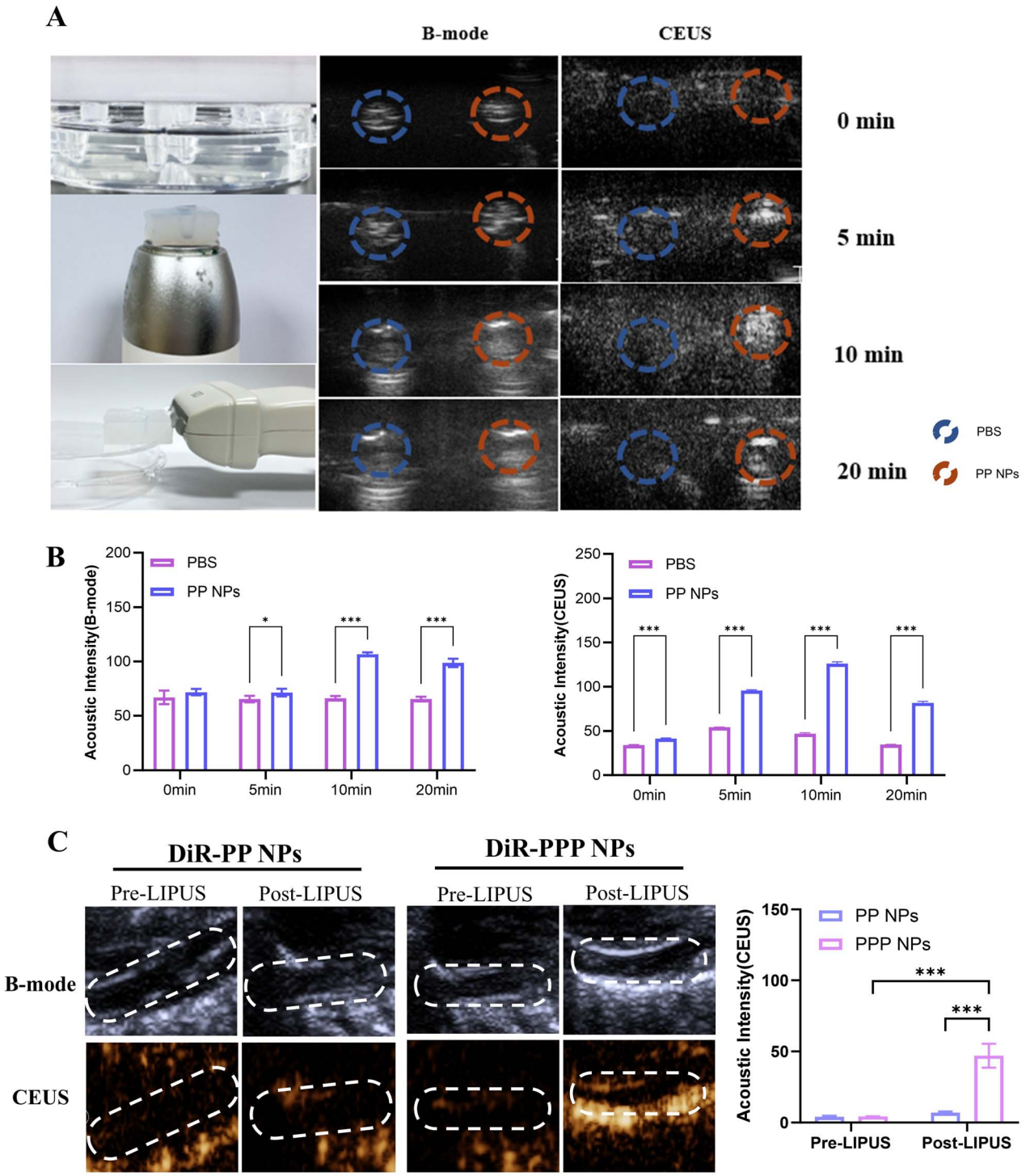

Fig. 3 *In vitro*/vivo ADV effect of NPs (A) Schematic illustration of agarose module preparation, accompanied by representative B-mode and CEUS images of PP NPs and PBS control before and after LIPUS irradiation. (B) Quantitative comparison of B-mode gray values and CEUS signal intensity between the two groups at each time point (*$P < 0.05$, ***$P < 0.001$). (C) Representative B-mode and CEUS images demonstrating the *in vivo* ADV effects following LIPUS irradiation in the presence of targeted *versus* non-targeted NPs. And comparative evaluation of CEUS signal intensity changes pre- and post-LIPUS irradiation, showing significant enhancement in the targeted NPs group (***$P < 0.001$). ADV: Acoustic droplet vaporization, CEUS: Contrast-enhanced ultrasound, NPs: Nanoparticles, PBS: Phosphate-buffered saline, LIPUS: Low-intensity pulsed ultrasound.

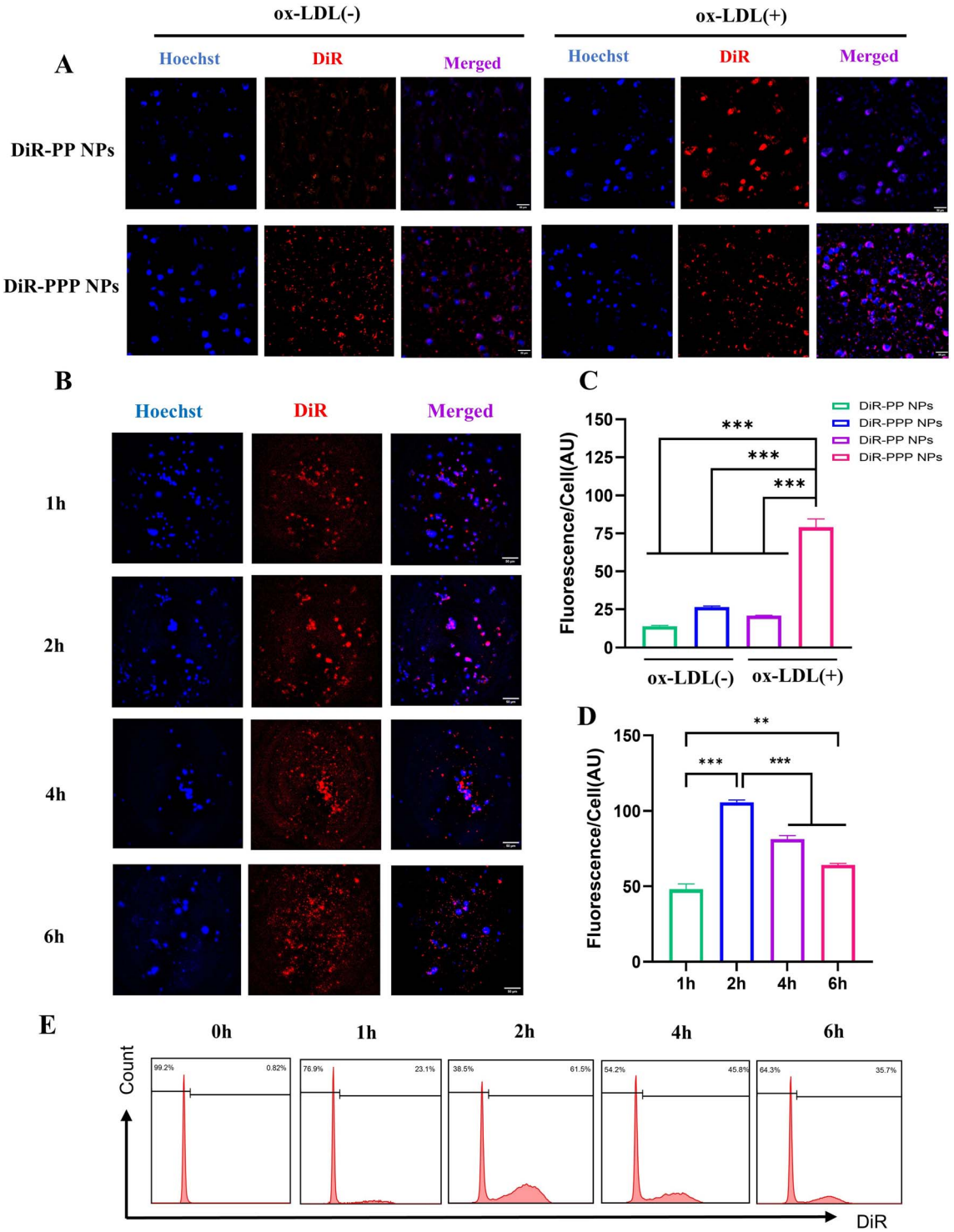

Fig. 4 Targeted and uptake efficiency of NPs *in vitro* (A) Representative fluorescence microscopy images demonstrating the binding capacity of PP NPs and PPP NPs to RAW 264.7 macrophages and foam cells. (scale bar = 50 μm) (B) Fluorescence microscopy observations of RAW 264.7 cell uptake of PPP NPs at different time point. (scale bar = 50 μm) (C) Analysis of fluorescence intensity of targeting capacity. (D) Analysis of fluorescence intensity of cell uptake at different time. (E) Flow cytometry analysis of the rate of NPs uptake by cells of different time point. NPs: Nanoparticles.

Evaluation of treatment effectiveness

***In vitro* treatment effect.** To evaluate the effect of PPP@RAP NPs combined with LIPUS on macrophage foaminess, ORO staining revealed that both NPs group and the LIPUS group significantly reduced lipid droplet accumulation compared to untreated foam cells. Notably, the combined treatment group exhibited a more pronounced reduction ($P < 0.01$) (SI Fig. S1D and E). We assessed the mRNA expression of TNF-α, IL-1β and

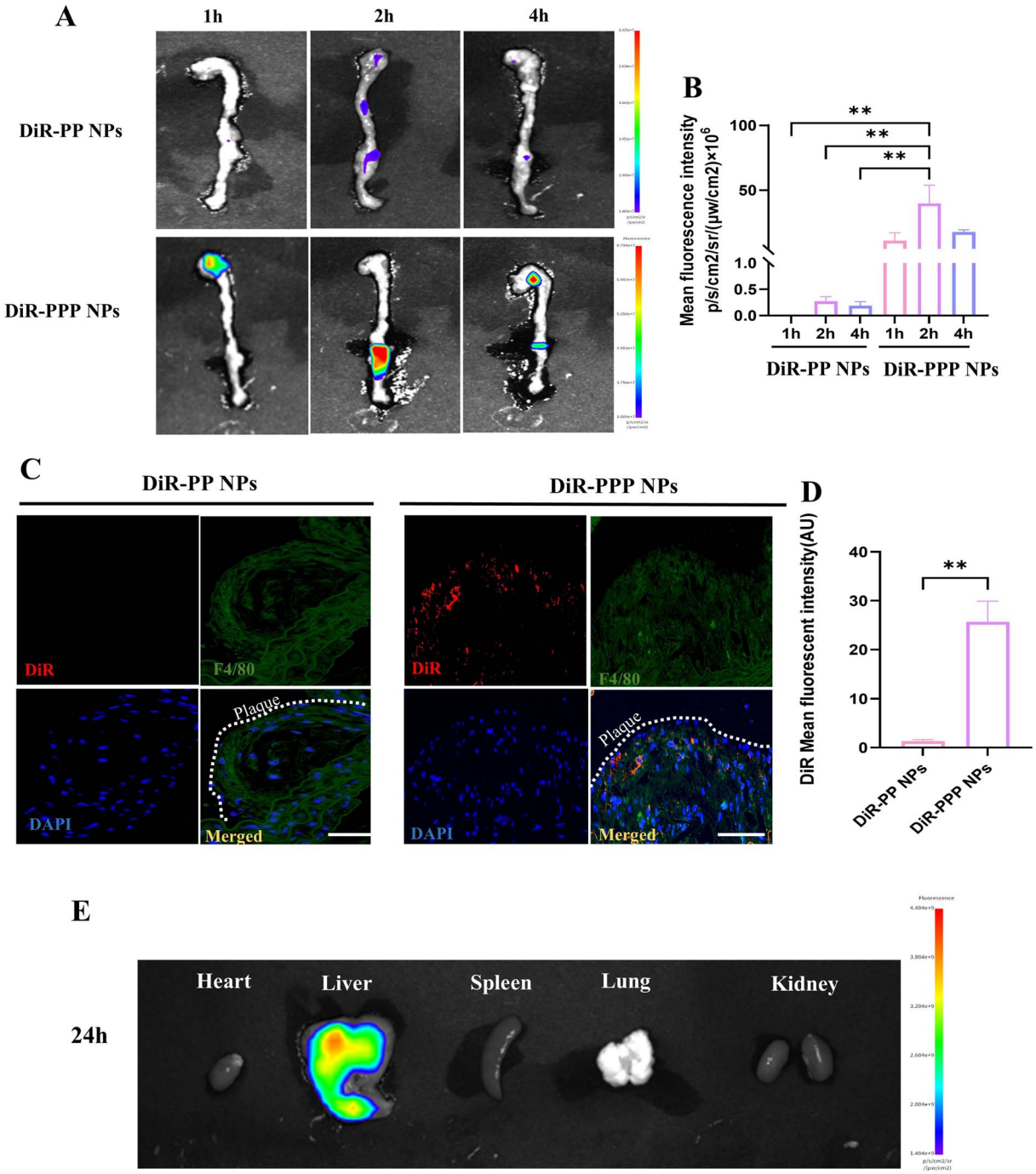

Fig. 5 Targeted efficiency of NPs *in vivo* (A) Fluorescence imaging of isolated aortas from atherosclerotic model mice following intravenous administration of PP NPs and PPP NPs. (B) Comparative analysis of fluorescence intensity in isolated aortas, showing significantly enhanced accumulation of PPP NPs compared to PP NPs (**$P < 0.01$). (C) Multiplex immunofluorescence imaging of tissue sections showing co-localization of DiR-labeled NPs (red) with F4/80+ macrophages (green) and nuclear staining (DAPI, blue) in targeted *versus* non-targeted groups. (Scale bar = 100 μm). (D) Comparative analysis of fluorescence intensity in plaque lesion, showing significantly enhanced accumulation of PPP NPs compared to PP NPs (**$P < 0.01$). (E) Fluorescence intensity distribution in major organs (heart, liver, spleen, lungs, and kidneys) 24 h post-injection of PPP NPs. NPs: Nanoparticles. DAPI: 4,6-diamidino-2-phenyindole dilactate, DiR: 1,1′-dioctadecyl-3,3,3′,3′-tetramethylindotricarbocyanine iodide.

iNOS in foam cells by qPCR assay to determine whether the combined treatment could reduce the inflammatory level of foam cells. The qPCR results demonstrated that the mRNA expression levels of inflammatory factors in foam cells were significantly downregulated ($P < 0.05$) following the combination treatment (SI Fig. S1F).

***In vivo* treatment effects.** During the treatment period, we regularly measured the body weight of the mice and closely

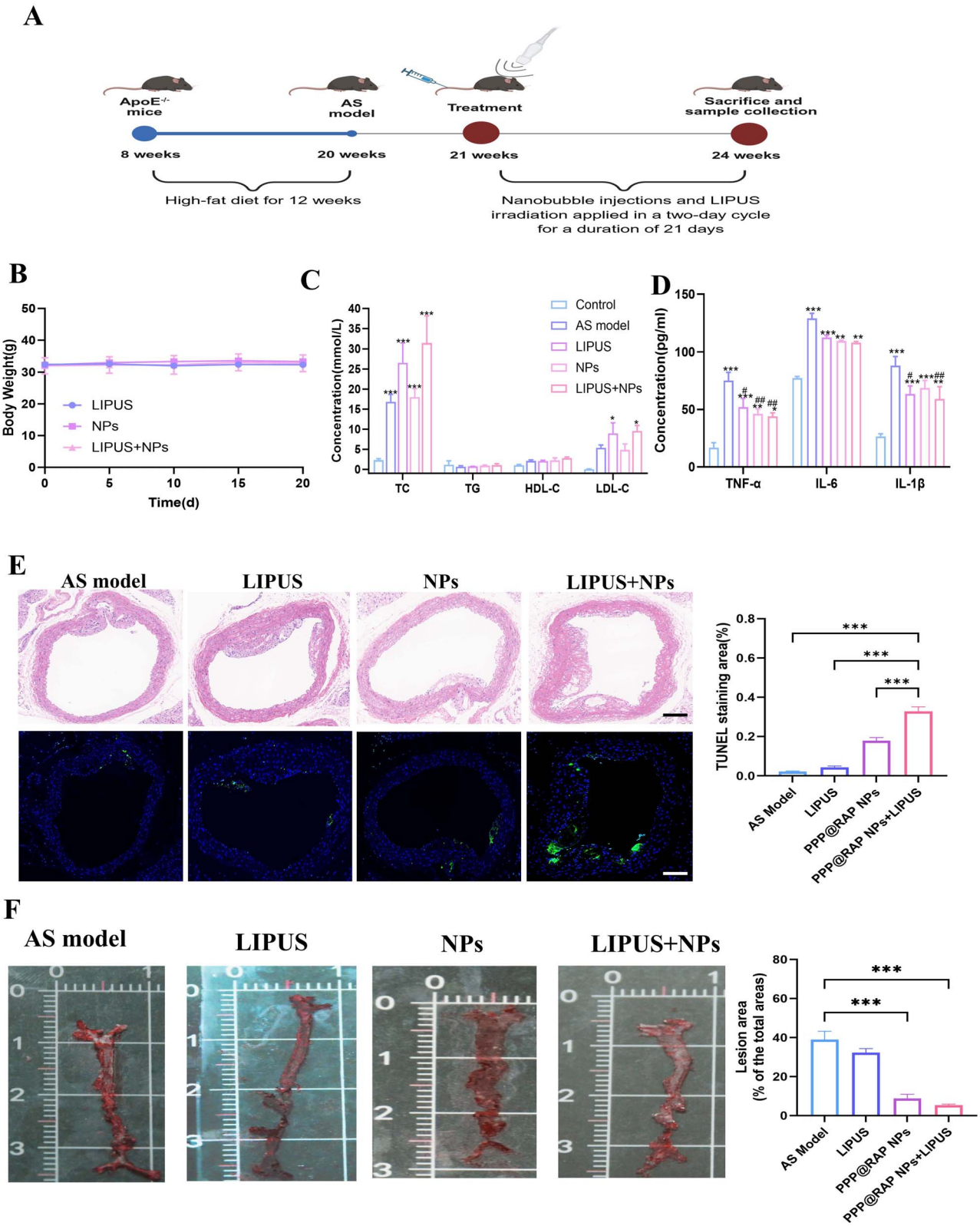

Fig. 6 Therapeutic Efficacy of PPP@RAP NPs Combined with LIPUS *in vivo* (A) Schematic timeline illustrating the treatment protocol. (B) Longitudinal assessment of body weight changes in different treatment groups throughout the intervention period. (C) Comparative evaluation of serum lipid parameters (TC, TG, LDL-C, HDL-C) among treatment groups. (*P < 0.05, **P < 0.01, ***P < 0.001 *versus* control group) (D) Changes in relevant inflammatory factors in mice before and after treatment. (*P < 0.05, **P < 0.01, ***P < 0.001 *versus* control; $^{\#}P$ < 0.05, $^{\#\#}P$ < 0.01 *versus* AS model group) (E) Representative images of H&E staining and TUNEL staining of aortic plaques, with quantitative analysis of apoptotic cell percentage (Scale bars: 100 μm). (***P < 0.001). (F) ORO staining of aortic gross specimens after treatment in each group of mice, with quantitative analysis of plaque area in entire aortas (***P < 0.001). NPs: Nanoparticles, LIPUS: Low-intensity pulsed ultrasound, ORO: Oil Red O, AS: Atherosclerosis, H&E: Hematoxylin and eosin, TUNEL: TdT-mediated dUTP nick-end labeling.

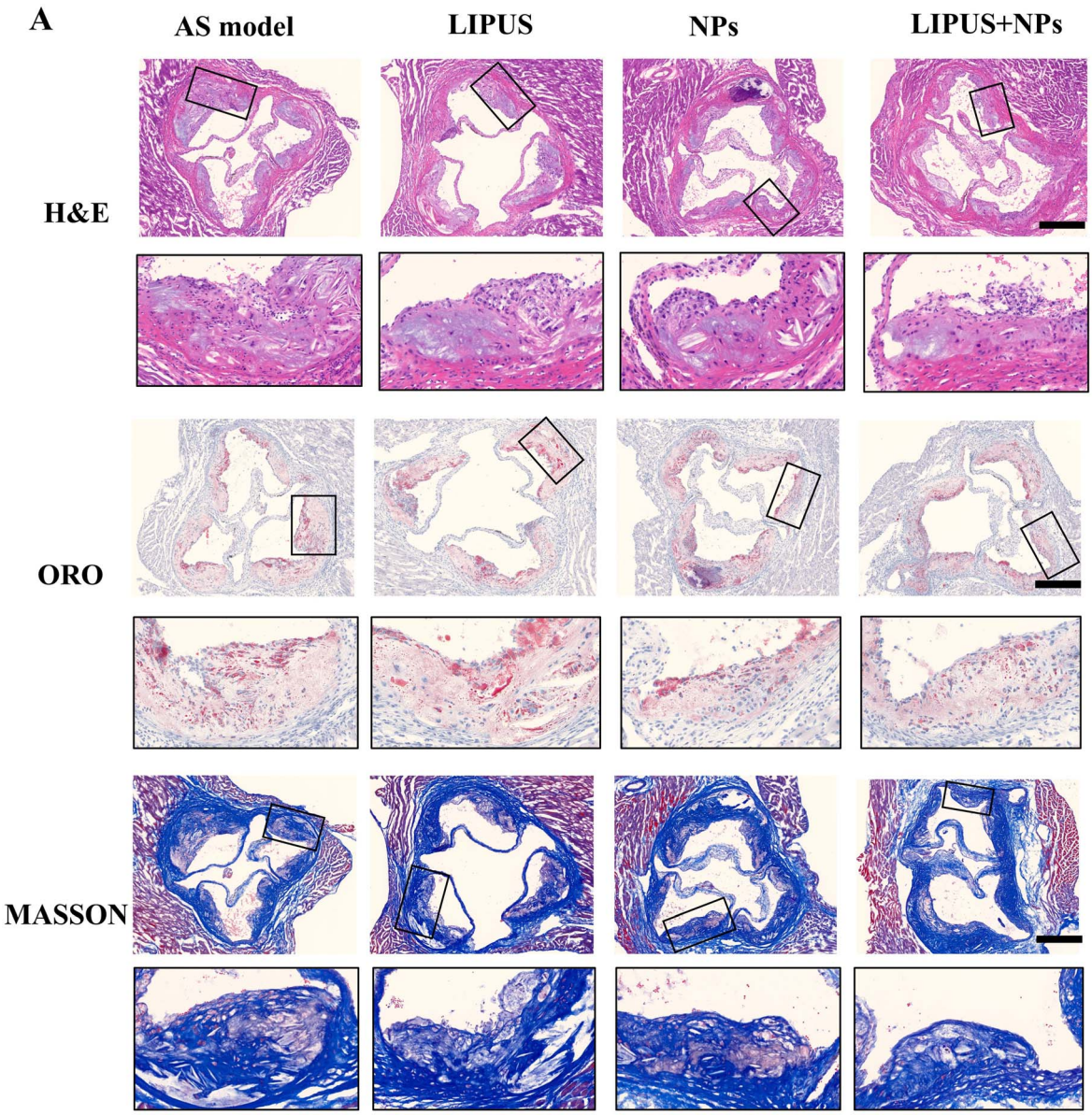

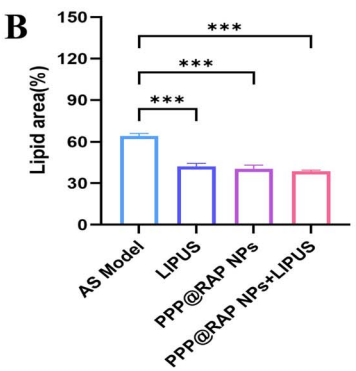

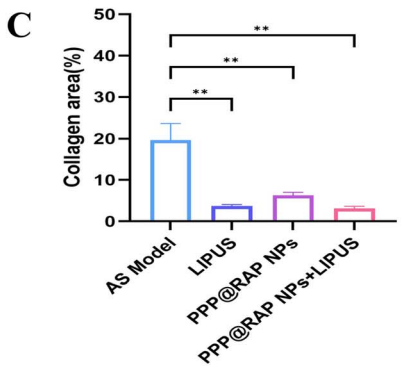

Fig. 7 Treatment effects in each group of mice (A) Images of aortic root sections stained with H&E, ORO, and Masson's trichrome (Scale bars: 100 μm). (B and C) Quantitative analysis of atherosclerotic plaque characteristics. Comparative evaluation of lipid content (ORO-positive area) and collagen deposition (Masson's trichrome-positive area) in aortic root sections among treatment groups (**P < 0.01, ***P < 0.001). NPs: Nanoparticles, LIPUS: Low-intensity pulsed ultrasound, AS: Atherosclerosis, ORO: Oil Red O, H&E: Hematoxylin and eosin.

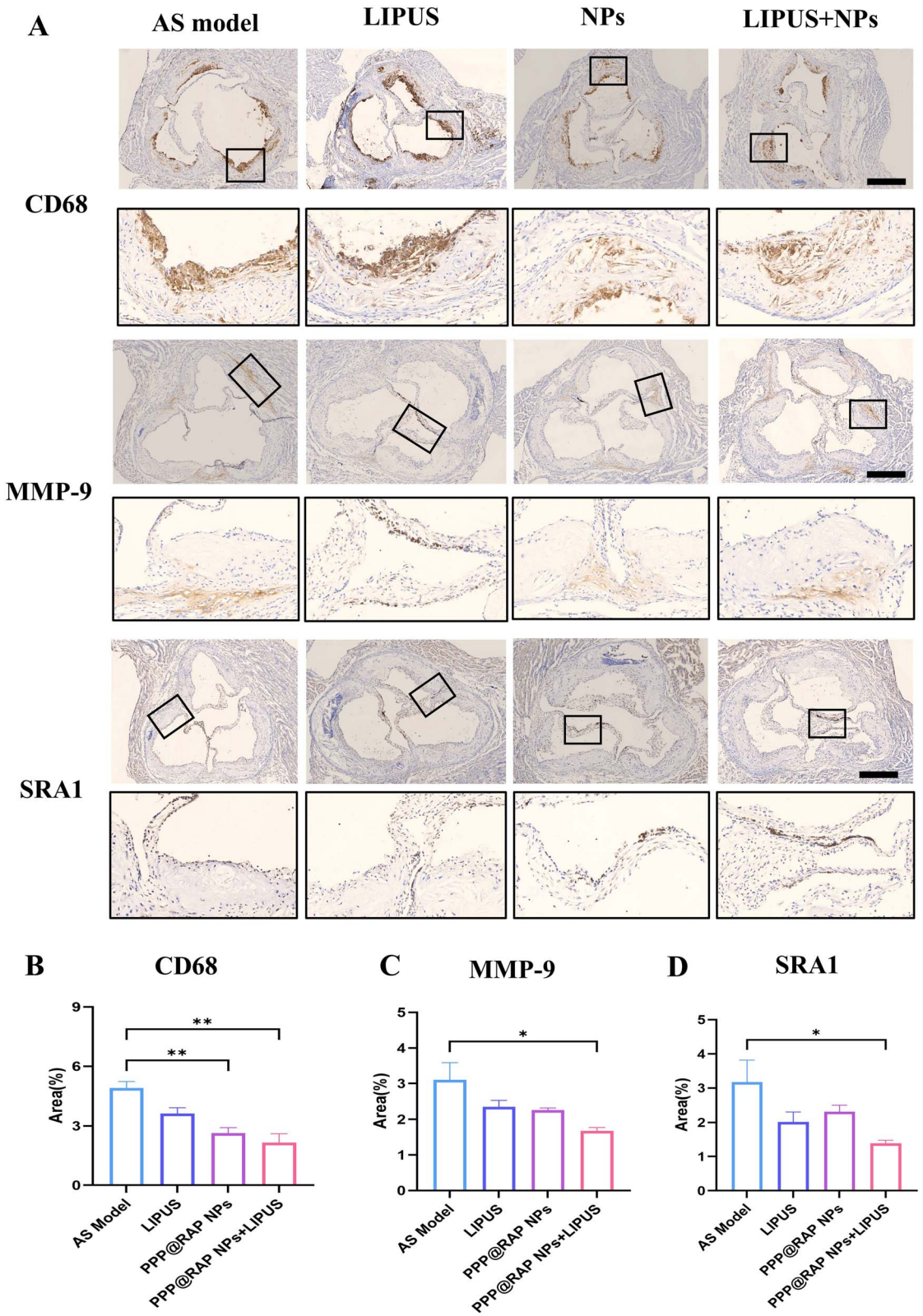

Fig. 8 Immunohistochemical analysis of atherosclerotic plaque composition in different treatment groups (A) Representative images of aortic root sections stained for macrophages (CD68), MMP-9, and SRA1 in different treatment groups (Scale bars: 100 μm). (B–D) Comparative evaluation of positive staining areas for CD68, MMP-9, and SRA1 in aortic root plaques among treatment groups (*P < 0.05, **P < 0.01). NPs: Nanoparticles, LIPUS: Low-intensity pulsed ultrasound, AS: Atherosclerosis.

monitored their general health status. No significant changes in body weight were observed across all groups of mice (Fig. 6B), and the mice were in good general condition. The lipid levels (TC, TG, HDL-C and LDL-C) of mice in each group did not show significant changes after treatment (Fig. 6C). ELISA results showed that the levels of inflammatory factors in all the groups were significantly decreased compared to the model group ($P < 0.05$) (Fig. 6D). Initially, the gross specimens were collected for ORO staining, and the plaque area was quantitatively analyzed (Fig. 6F). It was found that the percentage of plaque area in the whole aorta of the combined treatment group was significantly reduced than that in the model group (5.35% & 38.99%), representing a statistically significant difference ($P < 0.001$). Subsequent histopathologic staining of aortic root plaques was conducted to evaluate treatment efficacy (Fig. 7A). After 21 days of treatment, both the lipid area and collagen area in the combination therapy group were significantly smaller than those in the model group ($P < 0.001$) (Fig. 7B and C), with reductions of 25.99% and 16.48%, respectively. H&E and TUNEL staining of plaque lesion sites were performed to assess cell apoptosis in different treatment groups. The apoptosis rate in the combination treatment group significantly increased than other groups ($P < 0.001$) (Fig. 6E). Immunohistochemical staining (Fig. 8A) showed that the expression levels of CD68, MMP-9, and SR-A1 were decreased in the combined treatment group compared to the model group ($P < 0.05$) (Fig. 8B–D).

Discussion

NPs characterization and drug release evaluation

Particle size is a crucial parameter influencing the *in vivo* behavior of NPs.[21] The PPP@RAP NPs synthesized in this study, with an average diameter of (162.63 ± 3.25) nm, fall within the ideal range of 50–200 nm. TEM results further confirmed that the conjugation of peptides and the incorporation of the drug did not alter the overall spherical morphology of the nanoparticles, but primarily contributed to the increase in particle size. This result is of great significance, too small particle size is easily cleared by the kidney,[22] while too large size may activate the complement system and be rapidly cleared from the blood.[23] Consistent with the findings reported by Pang *et al.*[24] that NPs with a particle size of 80–200 nm showed good *in vivo* circulation stability. The negatively charged surface (−28.3 ± 0.46 mV) and PLGA matrix reduce reticuloendothelial system (RES)-mediated clearance and interparticle aggregation.[21] This surface charge and structural integrity are maintained across various physiological media, ensuring prolonged blood circulation and targeted delivery. The spherical morphology with a smooth surface, confirmed by TEM, minimizes nonspecific interactions *in vivo*, enhancing the NPs' stability and bioavailability.

This study prepared drug-loaded NPs by referring to dichloromethane co-dissolution method reported by Li *et al.*[25] and further optimized the preparation process. Leveraging the excellent hydrophobic compatibility between RAP and PLGA, and combining with PVA-assisted solvent emulsification, efficient encapsulation was achieved. The LC reached (36.95 ± 0.01)%, and the EE was (64.67 ± 0.01)%, surpassing traditional PLGA NPs (typical LC <30%). The LIPUS-triggered three-stage release mechanism is noteworthy: initial surface drug release occurred within 4 hours, followed by an accelerated release phase due to the phase transition of PFP and the formation of micropores in the PLGA shell. The cumulative release rate reached 69.30% at 72 hours, outperforming traditional PLGA NPs (20–25%) while avoiding burst release, thus extending the therapeutic duration. This result is consistent with most findings in the current literature.[26–29] The ADV effect further enhances inertial cavitation, significantly increasing drug release.[30]

Assessment of the ADV effect

LIPUS irradiation (100 mW cm^{-2}) induced a time-dependent increase in acoustic intensity for PP NPs, peaking at 10 min in both B-mode and CEUS imaging. The phase transition process of NPs is similar to the result of Guo's team.[31] This phenomenon is attributed to the liquid–gas phase transition of PFP within the NPs and the rupture of particles caused by the mechanical force of ultrasound. The accumulation of phase-transition microbubbles and the rupture of NPs jointly led to a nonlinear increase in the acoustic signal. The decrease in acoustic intensity at 20 minutes may be due to the compromised structural integrity of NPs after ultrasound excitation, leading to a reduction in the effective concentration of NPs in the solution. It is noteworthy that the weak signal observed in the PBS group was spatially diffuse, and highly variable across samples, indicating non-specific interference likely arising from transient microbubbles during injection or inherent noise under high-sensitivity imaging settings. Parameter selection is based on *in vitro* screening of the system (SI Table S3) to ensure optimal efficacy and biosafety. Ultrasound imaging of ADV effects reveals that LIPUS irradiation at 2 hours post-injection NPs triggers a 85.64% increase in CEUS contrast intensity for targeted NPs, significantly higher than non-targeted NPs. This enhancement stems from SR-A1 mediated NPs enrichment in plaques provides a higher local concentration for phase transition and LIPUS-induced PFP vaporization generates microbubbles with high acoustic impedance, amplifying scattering signals. Immunofluorescence confirmed DiR-PPP NP co-localization with plaque macrophages, demonstrating a dual strategy combining active targeting for spatial precision and ultrasound responsiveness for temporal control, thereby addressing key challenges in atherosclerosis therapy.

Targetability evaluation

The targetability evaluation reveals a synergistic design strategy integrating peptide-mediated active targeting with LIPUS-responsive phase transition, demonstrating precise spatiotemporal control over NP accumulation and therapeutic activation. *In vitro* imaging confirms PP1-conjugated NPs (DiR-PPP NPs) specifically bind foam cells *via* SR-A1 recognition, while non-targeted PP NPs show minimal uptake. Although a slight fluorescence increase in RAW 264.7 cells uptake PPP NPs was observed, likely due to heterogeneous receptor expression in polarized macrophages leading to non-specific binding. This specificity highlights the critical role of PP1 peptide in

mediating receptor-mediated endocytosis, which aligns with Gu's research showing that ligand-functionalized NPs enhance plaque accumulation compared to non-targeted counterparts.[32] The absence of off-target binding in normal cells underscores the strategy's potential to minimize systemic toxicity.

In vivo studies in ApoE$^{-/-}$ mice further validate the targeting efficiency. DiR-PPP NPs achieve peak aortic accumulation at 2 hours post-injection, which correlated with the distribution dynamics of SR-A, a highly expressed target in plaque-associated foam cells. The higher fluorescence intensity in the targeted group compared to non-targeted NPs ($P < 0.01$) indicates that active targeting significantly improves plaque residency, which is critical for therapeutic efficacy. Fluorescence imaging after systemic administration revealed widespread signal distribution across aortic segments, consistent with the systemic nature of atherosclerosis. Although plaque formation exhibits high-incidence regions, it is not confined to a single location. Variations in fluorescence intensity likely reflect heterogeneity in local pathological features, including differences in plaque burden (larger lipid cores), inflammatory states (elevated SR-A1 expression), and plaque stability (stronger nanoparticle retention in rupture-prone areas). It is important to emphasize that no ultrasound-guided localization was performed prior to injection in this experiment. The results directly demonstrate the inherent active targeting capability of DiR-PPP NPs to autonomously accumulate in atherosclerotic lesions following systemic circulation, aligning with the experimental objective of validating lesion-specific targeting without external intervention.

This temporal dynamics study establishes a precise window for LIPUS application. The predominant NP accumulation in the liver at 24 hours, a typical RES clearance pathway, suggests minimal off-target organ toxicity.

Evaluation of treatment effectiveness

The combined therapy of PPP@RAP NPs and LIPUS demonstrates multifaceted therapeutic effects against atherosclerosis, integrating lipid regulation, anti-inflammation, and plaque stabilization. *In vitro* studies reveal that the combination treatment reduces lipid droplet accumulation in foam cells compared to monotherapy groups, accompanied down-regulation of proinflammatory cytokines. This synergistic effect stems from LIPUS-triggered PFP phase transition for controlled rapamycin release. The dual action on lipid metabolism and inflammation aligns with the "lipid-inflammatory crosstalk" hypothesis in atherosclerosis.[33]

In vivo evaluations in ApoE$^{-/-}$ mice show that the combination therapy reduces aortic plaque area by 86% (combined group 5.35% *vs.* AS model group 38.99%), with concurrent decreases in lipid content and collagen deposition. The enhanced foam cell apoptosis may attributed to the fact that liquid droplets have stronger tissue penetration than conventional light during phase-change activation,[34] inducing apoptosis of foam cells in plaques. The presence of TUNEL-positive signals overlapping with the vascular wall structure also suggests treatment-induced apoptosis localized to the plaque area, likely resulting from ultrasound-enhanced targeted drug delivery and release. Importantly, no significant structural damage to the vasculature was observed, indicating that the apoptotic effects are treatment-specific rather than indicative of non-specific injury. The combined treatment also down-regulated CD68, MMP-9, and SR-A1 expression, indicating reduced macrophage infiltration and improved plaque stability. And the positive correlation between MMP-9 level and plaque instability[35] that the decreased MMP-9 expression demonstrates the ability of the combination treatment to stabilize atherosclerotic plaques. However, voids observed in H&E staining suggest rapid lipid clearance that exceeds the rate of tissue repair, highlighting the need to assess long-term mechanical stability and incorporate key vulnerability indicators such as fibrous cap thickness and plaque burden/fibrous cap thickness ratio. In the future, we should also evaluate VSMC marker and apoptosis molecules, and quantify intraplaque RAP *via* LC-MS/MS to correlate release kinetics with efficacy. Consequently, it is imperative to conduct comprehensive safety evaluations, integrating plaque-related vulnerability indicators to ensure the overall safety of the treatment and highlighting the need for long-term studies on plaque mechanical stability.

The translational potential of this approach is underscored by its spatiotemporal precision: NPs targeting to SR-A1 in foam cells ensures local drug concentration, while LIPUS activation enables on-demand release with minimal systemic exposure. Compared to traditional statin therapy, which primarily reduces circulating lipids, this strategy offers plaque-specific intervention, as evidenced by unchanged systemic lipid profiles in treated mice. However, challenges remain, including optimizing LIPUS parameters to balance cavitation efficiency and plaque stability, as well as addressing potential off-target effects of rapamycin on wound healing. Future studies should explore nanocarrier modifications to enhance fibrotic cap reinforcement and evaluate the therapy in models of vulnerable plaques.

Conclusion

In summary, this study establishes a paradigm for integrating targeted nanodelivery with ultrasound-responsive release, demonstrating that can concurrently regress plaques and improve their mechanical stability. The nanosystem also showed excellent biosafety, with no significant toxic side effects observed during long-term administration. This innovative strategy offers a new approach to targeted cardiovascular therapy, with significant potential for clinical translation and future research.

Author contributions

D.-W.: writing–original draft, investigation, conceptualization; X.-Z.: writing–original draft, investigation; L.-T.: writing–original draft, investigation; S.-W.: investigation, Y.-H.: investigation, J.-L.: investigation, Y.-W.: investigation, S.-Z.: investigation, J.-L.: writing – review and editing; G.-L.: writing – review and editing. The manuscript was written through contributions of all authors. All authors have given approval to the final version of the manuscript.

Conflicts of interest

The authors declare that they have no competing interests.

Abbreviations

AS	Atherosclerosis
ADV	Acoustic droplet vaporization
CEUS	Contrast-enhanced ultrasound
DAPI	4,6-Diamidino-2-phenyindole dilactate
DEG	Differentially expressed genes
DiR	1,1′-Dioctadecyl-3,3,3′,3′-tetramethylindotricarbocyanine iodide
DLS	Dynamic light scattering
EDC	1-Ethyl-3-(3-dimethyllaminopropyl)-carbodiimide hydrochloride
EE	Encapsulation efficiency
ELISA	Enzyme-linked immunosorbent assay
ET	Exposure time
FBS	Fetal bovine serum
FDR	False discovery rate
FITC	Flurescein isothiocyanate
H&E	Hematoxylin and eosin
HFD	High-fat diet
I_{SATA}	Spatial-average temporal-average intensity
KEGG	Kyoto Encyclopedia of Genes and Genomes
LC	Loading capacity
LIFU	Low-intensity focused ultrasound
LIPUS	Low-intensity pulsed ultrasound
NHS	*N*-Hydroxysuccinimide
NPs	Nanoparticles
ORO	Oil red O
ox-LDL	Oxidized low-density lipoprotein
PBS	Phosphate-buffered saline
PDI	Polydispersity index
PFCs	Perfluorocarbons
PFP	Perfluoropentane
PVA	Polyvinyl alcohol
PPI	Protein–protein interaction
RAP	Rapamycin
SR-A	Scavenger receptor A
TEM	Transmission electron microscope
TUNEL	TdT-mediated dUTP nick-end labeling

Data availability

The data supporting this article have been included as part of the supplementary information (SI). Supplementary information: sequence of primers, characterization, exploration of optimal LIPUS parameters, *in vitro* treatment and other additional results. See DOI: https://doi.org/10.1039/d5ra09347c.

Acknowledgements

The graphic abstract and Fig. 6A were created by Biorender (https://www.biorender.com/). We are grateful to the Medical Research Center of Quanzhou Medical College for the conduct of the experiments. This work was supported by Special Fund for Doctoral Supervisors of the Second Affiliated Hospital of Fujian Medical University (grant no. 2024BD1102).

References

1 L. E. Mantella, K. Liblik and A. M. Johri, Vascular imaging of atherosclerosis: Strengths and weaknesses, *Atherosclerosis*, 2021, **319**, 42–50.
2 P. Libby, J. E. Buring, L. Badimon, *et al.*, Atherosclerosis, *Nat Rev Dis Primers*, 2019, **5**(1), 56.
3 A. R. Tall and R. L. Levine, Cardiovascular disease: Commonality with cancer, *Nature*, 2017, **543**(7643), 45–47.
4 M. Naghavi, P. Libby, E. Falk, *et al.*, From vulnerable plaque to vulnerable patient: a call for new definitions and risk assessment strategies: Part I, *Circulation*, 2003, **108**(14), 1664–1672.
5 J. Fan and T. Watanabe, Atherosclerosis: Known and unknown, *Pathol Int*, 2022, **72**(3), 151–160.
6 R. A. Byrne, M. Joner and A. Kastrati, Stent thrombosis and restenosis: what have we learned and where are we going? The Andreas Gruntzig Lecture ESC 2014, *Eur Heart J*, 2015, **36**(47), 3320–3331.
7 W. Chen, M. Schilperoort, Y. Cao, *et al.*, Macrophage-targeted nanomedicine for the diagnosis and treatment of atherosclerosis, *Nat Rev Cardiol*, 2022, **19**(4), 228–249.
8 C. Gao, Q. Huang, C. Liu, *et al.*, Treatment of atherosclerosis by macrophage-biomimetic nanoparticles *via* targeted pharmacotherapy and sequestration of proinflammatory cytokines, *Nat. Commun.*, 2020, **11**(1), 2622.
9 R. Duivenvoorden, J. Tang, D. P. Cormode, *et al.*, A statin-loaded reconstituted high-density lipoprotein nanoparticle inhibits atherosclerotic plaque inflammation, *Nat. Commun.*, 2014, **5**, 3065.
10 Y. Liu, F. Yang, S. Zou, *et al.*, Rapamycin: A Bacteria-Derived Immunosuppressant That Has Anti-atherosclerotic Effects and Its Clinical Application, *Front. Pharmacol*, 2018, **9**, 1520.
11 T. L. Kaeberlein, A. S. Green, G. Haddad, *et al.*, Evaluation of off-label rapamycin use to promote healthspan in 333 adults, *Geroscience*, 2023, **45**(5), 2757–2768.
12 O. D. Kripfgans, J. B. Fowlkes, D. L. Miller, *et al.*, Acoustic droplet vaporization for therapeutic and diagnostic applications, *Ultrasound Med Biol*, 2000, **26**(7), 1177–1189.
13 C. A. Sennoga, E. Kanbar, L. Auboire, *et al.*, Microbubble-mediated ultrasound drug-delivery and therapeutic monitoring, *Expert Opin Drug Deliv*, 2017, **14**(9), 1031–1043.
14 Y. Zhong, Y. Zhang, J. Xu, *et al.*, Low-Intensity Focused Ultrasound-Responsive Phase-Transitional Nanoparticles for Thrombolysis without Vascular Damage: A Synergistic Nonpharmaceutical Strategy, *ACS Nano*, 2019, **13**(3), 3387–3403.
15 N. Jiang, B. Hu, S. Cao, *et al.*, Stable Low-Dose Oxygen Release Using H(2)O(2)/Perfluoropentane Phase-Change Nanoparticles with Low-Intensity Focused Ultrasound for Coronary Thrombolysis, *Ultrasound Med Biol*, 2020, **46**(10), 2765–2774.

16 P. N. Di, G. Formoso and A. Pandolfi, Physiology and pathophysiology of oxLDL uptake by vascular wall cells in atherosclerosis, *Vascul Pharmacol*, 2016, **84**, 1–7.
17 D. An, F. Hao, C. Hu, *et al.*, JNK1 Mediates Lipopolysaccharide-Induced CD14 and SR-AI Expression and Macrophage Foam Cell Formation, *Front Physiol*, 2017, **8**, 1075.
18 D. Ding and Q. Zhu, Recent advances of PLGA micro/nanoparticles for the delivery of biomacromolecular therapeutics, *Mater Sci Eng C Mater Biol Appl*, 2018, **92**, 1041–1060.
19 A. Ainiwan, Y. Wei, J. Dou, *et al.*, Functional evaluation of constructed pseudo-endogenous microRNA-targeted myocardial ultrasound nanobubble, *Front Med (Lausanne)*, 2023, **10**, 1136304.
20 X. Jiang, O. Savchenko, Y. Li, *et al.*, A Review of Low-Intensity Pulsed Ultrasound for Therapeutic Applications, *IEEE Trans Biomed Eng*, 2019, **66**(10), 2704–2718.
21 A. Albanese, P. S. Tang and W. C. Chan, The effect of nanoparticle size, shape, and surface chemistry on biological systems, *Annu. Rev. Biomed. Eng.*, 2012, **14**, 1–16.
22 H. S. Choi, W. Liu, P. Misra, *et al.*, Renal clearance of quantum dots, *Nat. Biotechnol.*, 2007, **25**(10), 1165–1170.
23 N. Hoshyar, S. Gray, H. Han, *et al.*, The effect of nanoparticle size on *in vivo* pharmacokinetics and cellular interaction, *Nanomedicine (Lond).*, 2016, **11**(6), 673–692.
24 H. Li, K. Jin, M. Luo, *et al.*, Size Dependency of Circulation and Biodistribution of Biomimetic Nanoparticles: Red Blood Cell Membrane-Coated Nanoparticles, *Cells*, 2019, **8**(8), 881.
25 G. Li, F. Xu, B. Yang, *et al.*, A nanotherapy responsive to the inflammatory microenvironment for the dual-targeted treatment of atherosclerosis, *Nanomedicine*, 2022, **43**, 102557.
26 H. Qin, R. Teng, Y. Liu, *et al.*, Drug Release from Gelsolin-Targeted Phase-Transition Nanoparticles Triggered by Low-Intensity Focused Ultrasound, *Int J Nanomedicine*, 2022, **17**, 61–71.
27 Y. Cao, Y. Chen, T. Yu, *et al.*, Drug Release from Phase-Changeable Nanodroplets Triggered by Low-Intensity Focused Ultrasound, *Theranostics*, 2018, **8**(5), 1327–1339.
28 Z. Liu, H. Ran, Z. Wang, *et al.*, Targeted and pH-facilitated theranostic of orthotopic gastric cancer *via* phase-transformation doxorubicin-encapsulated nanoparticles enhanced by low-intensity focused ultrasound (LIFU) with reduced side effect, *Int J Nanomedicine*, 2019, **14**, 7627–7642.
29 S. Huo, Z. Liao, P. Zhao, *et al.*, Mechano-Nanoswitches for Ultrasound-Controlled Drug Activation, *Adv. Sci.*, 2022, **9**(12), e2104696.
30 Q. Jin, S. T. Kang, Y. C. Chang, *et al.*, Inertial cavitation initiated by polytetrafluoroethylene nanoparticles under pulsed ultrasound stimulation, *Ultrason. Sonochem.*, 2016, **32**, 1–7.
31 J. Hou, J. Zhou, M. Chang, *et al.*, LIFU-responsive nanomedicine enables acoustic droplet vaporization-induced apoptosis of macrophages for stabilizing vulnerable atherosclerotic plaques, *Bioact Mater*, 2022, **16**, 120–133.
32 H. He, Q. Han, S. Wang, *et al.*, Design of a Multifunctional Nanozyme for Resolving the Proinflammatory Plaque Microenvironment and Attenuating Atherosclerosis, *ACS Nano*, 2023, **17**(15), 14555–14571.
33 S. C. de Jager and G. Pasterkamp, Crosstalk of lipids and inflammation in atherosclerosis: the PRO of PGRN?, *Cardiovasc. Res.*, 2013, **100**(1), 4–6.
34 R. Zhang, R. Liu, C. Liu, *et al.*, A pH/ROS dual-responsive and targeting nanotherapy for vascular inflammatory diseases, *Biomaterials*, 2020, **230**, 119605.
35 T. Li, X. Li, Y. Feng, *et al.*, The Role of Matrix Metalloproteinase-9 in Atherosclerotic Plaque Instability, *Mediators Inflamm*, 2020, **2020**, 3872367.